The 6 June 2003 Bardwell, Kentucky, Earthquake Sequence: Evidence for a Locally Perturbed Stress Field in the Mississippi Embayment

Stephen P. Horton[1], Won-Young Kim[2], and Mitch Withers[1]

[1] Center for Earthquake Research and Information,
University of Memphis

[2] Lamont-Doherty Earth Observatory of Columbia University,
Palisades, NY 10964

shorton@memphis.edu

For submission to
Bulletin of the Seismological Society of America
March 2004

Abstract

Detailed analysis of regional and local waveform data from the 6 June 2003 Bardwell, Kentucky, earthquake indicates that the mainshock has the seismic moment of M_0 =1.3 (±0.5) × 10^{15} N m (Mw 4.0) and occurred at a depth of about 2 (±1) km on a near-vertical fault plane. The focal mechanism is predominantly strike slip with a sub-horizontal P-axis trending 118º. A temporary seismic network recorded 85 aftershocks that delineate an east-trending fault approximately 1 km in length. In a north-south cross-section, the aftershocks illuminate a nearly vertical plane between 2.0 and 2.7 km depth in general agreement with the west-southwest striking nodal plane (dip=70º and strike=251º) of the mainshock focal mechanism. The aftershock cluster in the along-strike cross-section supports interpretation of the mainshock as a circular fault area with a radius of about 0.44 (±0.03) km. This source radius yields a static stress drop of $\Delta\sigma$ = 67 (±14) bars for the mainshock. A formal stress inversion based on the focal mechanisms of the mainshock and ten aftershocks indicates the maximum compressive stress trends 104° with a plunge of 5°. The local stress field near Bardwell is therefore rotated around 40° clockwise relative to 65° for eastern North America as a whole. The Bardwell earthquakes have the opposite sense of slip to earthquakes with east-trending nodal planes that occur near New Madrid, Missouri. This requires a significant local rotation of the stress field over a distance of 60 km.

Introduction

On 6 June 2003 at 12:29 (UTC), a moderate-sized (Mw 4) earthquake occurred near Bardwell, Kentucky (Figure 1). Bardwell is approximately 57 km northeast of New Madrid, Missouri, in an area of transition from the northeast-trending Reelfoot rift to the east-trending Rough Creek graben. The Bardwell mainshock was felt in western Kentucky and parts of Tennessee, Missouri, and Indiana. Ground acceleration recorded in Wickliffe, Kentucky, approximately 13 km from the epicenter, attained a peak of 0.02g (Wang et al., 2003). Minor damage was reported in and around the town of Bardwell. Bricks fell from a two-story masonry building in the center of town. An archway in the courthouse sustained cracks in the mortar and some broken bricks. A portion of the ceiling collapsed in the local Dollar General Store. Several residents of Bardwell reported that a loud explosive sound preceded strong shaking. A county judge heard a "low rumble" turn into a "deafening roar" right before the earthquake hit. The shaking was strong enough to encourage some residents to exit their houses and to cause some difficulty in standing.

Within 15 hours after the mainshock, a temporary network of five broadband seismographs had been installed in the epicentral area to record aftershocks. Although an Mw 4 earthquake is rather small to warrant the effort for an aftershock study, this is one of the two largest earthquakes to occur in the Mississippi embayment since the upgrade of the regional seismic network beginning in 1998. A four-week long aftershock survey captured 85 aftershocks that produced high-quality 3-component broadband seismic records. The aftershocks are tightly clustered and have magnitude up to 2.4. Thus the mainshock and aftershocks provide unique data for the study of seismic wave propagation in deep soils and tectonic processes in an intra-plate region. In this paper, we characterize seismic sources and the local stress field.

A primary goal of the aftershock study is to determine the depth and fault geometry of the mainshock. The distribution of aftershocks derived from a standard single-event location method clearly defines an east-trending fault plane around 1 km in length and about 2.5 km underneath the town of Bardwell. However, the significance of the inferred fault geometry is diminished since location uncertainties are on the same order as the fault dimensions. To reduce the level of location uncertainty, we applied the double-difference earthquake location method (Waldhauser, 2001). The double-difference method promotes an order of magnitude improvement in uncertainty compared to single-event locations (Waldhauser and Ellsworth, 2000). After relocation, the mainshock fault geometry is determined with increased confidence. A fault radius

is estimated, and along with the seismic moment, is used to estimate the static stress drop for the mainshock.

A second goal of the aftershock study is to obtain an estimate of the orientation of the local stress field indicated by the mainshock and aftershocks of the Bardwell earthquake sequence. The focal mechanism of the mainshock is determined by regional waveform inversion and we obtained well-constrained focal mechanisms for ten aftershocks by using P-, SH- and SV-wave polarities and amplitude ratios of these phases. These focal mechanisms are the basis for a stress tensor inversion using the method developed by Gephart (1990).

In the following, we discuss the tectonic setting of the 2003 Bardwell, Kentucky, earthquake sequence, the estimation of the depth and focal mechanism of the mainshock from regional waveform inversion, aftershock locations and focal mechanisms, and constraints on the mainshock location. This is followed by a discussion of the local stress field.

Tectonic Setting

The 2003 Bardwell earthquake sequence occurs in the northern Mississippi embayment (Figure 1), a southwest plunging synclinal trough of poorly consolidated to unconsolidated sediments (Stearns, 1957). The synclinal axis roughly coincides with the present course of the Mississippi River. The Late Cretaceous to recent clastic sediments are around 340 m thick in the study area, thicken to around 1000 m near Memphis, and feather erosionally to zero thickness at the embayment margins (Dart, 1992). These sediments lie unconformably atop Paleozoic sedimentary rock. The Paleozoic rocks form a veneer several kilometers thick lying unconformably above the crystalline basement. The Precambrian basement is found at 4200 m depth in the Dow Chemical #1 Wilson drill hole (Howe, 1984) in southeastern Arkansas. The crystalline basement is part of a vast Proterozoic (1.48 -1.45 Ga) igneous province stretching from northern Mexico to eastern Quebec termed the “eastern granite-rhyolite province” (Bickford et al. 1986).

The structural framework of the study area is complex. The embayment sediments have a regional dip towards the south and towards the axis of the embayment trough (Stearns, 1957). However, the underlying Paleozoic rocks in the study area dip northeast towards the Illinois basin and away from the Ozark uplift and Pascola arch (Kolata et al., 1981). Precambrian basement outcrops in the St. Francis Mountains of the Ozark uplift, but the top of the Precambrian basement deepens progressively towards the Illinois basin (McBride et al., 2003).

The top of the Precambrian basement is between 3 and 4 km deep in the study area, and over 6 km deep near the Rough Creek fault.

Two rifts in the Precambrian basement occur in the study area. The northeast trending Reelfoot rift formed during a major extensional event in the late Precambrian or early Cambrian (Burke and Dewey, 1973) and reactivated during the Cretaceous to form the Mississippi embayment (Ervin and McGinnis, 1975). Gravity and magnetic anomalies are interpreted as a northeast-trending graben 70 km in width and more than 300 km in length with structural relief of about 2 km (Hildenbrand et al., 1977, 1982; Kane et al., 1981). The maximum depth to basement is about 5 km in the center of the rift and 3 km at the flanks (Kane et al., 1981; Ginzburg et al., 1983; Mooney et al., 1983; Hildenbrand, 1985). The Reelfoot rift may be underlain by a "rift pillow," a high-velocity and high-density crustal layer 30-40 km deep (Ginzburg et al., 1983; Mooney et al. 1983). Based on gravity and subsurface data, Soderberg and Keller (1981) suggest the east-trending Rough Creek graben is the same age and contiguous with the Reelfoot rift.

The New Madrid Seismic Zone (NMSZ) southwest of Bardwell in Figure 1 is strongly associated with the Reelfoot rift. Concentrated microseismic activity delineates two northeast-trending segments offset by a north-northwest-trending segment. In the southern segment, earthquakes are concentrated along the center of the Reelfoot rift axis. On the other hand, the northwest-trending segment actually cuts across the western rift boundary. The Reelfoot rift is the most seismically active of six Iapetan rifts and grabens in central and eastern North America, while the Rough Creek graben is one of the least active (Wheeler, 1997).

Three large earthquakes occurred in the NMSZ during the winter of 1811-1812. Paleoliquifaction evidence suggests five to nine magnitude 7-8 earthquakes have occurred in the NMSZ in the last 1100 years (Tuttle et al., 2002). Global positioning satellite observations indicate differential displacement rates less than 1-2 mm/yr (Newman et al., 1999; Santillan et al., 2002). The three largest earthquakes in the NMSZ since the regional seismic network was established in 1974 are the 25 March 1976, Marked Tree, Arkansas earthquake (mb(Lg) = 5.0; Herrmann, 1979), 26 September 1990, Cape Girardeau, Missouri earthquake (mb(Lg)= 4.7; Langston, 1994), and the 4 May 1991, Risco, Missouri earthquake (mb(Lg) = 4.6; Langston, 1994). These and other earthquakes that occurred in NSMZ are predominantly strike-slip faulting on steeply dipping nodal planes with sub-horizontal P-axes trending ENE-E (see Table 1).

As opposed to the well-defined seismicity patterns of the NMSZ, seismicity to the north in southern Illinois and Indiana is more dispersed. The largest instrumentally recorded earthquake in the region is the 9 November 1968, southern Illinois earthquake (Mw=5.3; Table 1). Munson et al. (1997) have found paleoliquifaction evidence in the southern halves of Illinois and Indiana for at least six large (Mw > 6.0) Holocene earthquakes.

Since the Late Cretaceous (70 Ma) to present, east-west trending horizontal compressive stress is the primary tectonic force in the epicentral region (Kolata & Nelson, 1991). This regional stress may reactivate faults in the crystalline basement within the Reelfoot rift and the surrounding area.

Mainshock Focal Mechanism and Depth from Waveform Inversion

The 6 June 2003, Bardwell, Kentucky, earthquake was well recorded by broadband seismographic stations in the central and eastern United States (Figure 1). Regional seismic records at 13 stations in the distance range from 59 to 463 km are used to determine the focal mechanism and depth. The observed records are modeled using a frequency-wavenumber (*f-k*) integration method for a point source embedded in a simple 1D crustal velocity model (Saikia, 1994). A central United States crustal model with four layers over a half-space is used (Herrmann, 1979). A grid-search waveform inversion technique (Zhao & Helmberger, 1994) is employed. This method matches observed seismograms against synthetics over discrete wave trains and allows relative time shifts between individual wave trains. The preferred solution minimizes the fitting error (E) in terms of the four source parameters: seismic moment (M_0), strike, dip, and rake (see Kim, 2003). A global minimum error is sought for a range of trial depths.

A common problem in modeling regional waves is inadequate knowledge of the crustal structure and the corresponding Green's functions. One approach is to remove high frequency body waves and model only the long-period surface waves at around 20 sec period, as discussed by Zhao & Helmberger (1994) and Tio & Kanamori (1995). We model the complete waveform including body waves and surface waves over the period range 8 and 20 sec for records at distances less than 200 km, and 10 and 30 sec for records at greater distances. The filtered records are dominated by fundamental mode Rayleigh and Love waves, but also include Pnl-waves. The P-wave first-motion data from eight stations is also added in the inversion to help

constrain the source mechanism. The inversion for focal mechanism parameters is carried out as a grid-search through the whole parameter space of strike, dip and rake.

Figure 2 shows the comparison between the observed and synthetic waveforms for the best-fit solution. The observed signals are very well matched by the synthetics. The time shifts (dt) required to align the 32 traces are mostly positive with an average of 0.9 sec and a maximum value of 2.3 sec, indicating that the crustal velocities used to calculate synthetics are slightly faster than the actual values for most paths from this event. The moment tensor inversion using a similar crustal model for the northeastern U.S. (Yang & Aggarwal, 1981; Du et al., 2003) produced almost identical results with time shifts of 0.8 sec.

The preferred focal mechanism (Figure 2) is dominantly strike-slip with near-vertical nodal planes. The best-fitting double-couple source parameters are strike = 251º, dip = 70º, rake = 165º, and seismic moment = 1.3 ($\pm$0.5) $\times$ 10^{15} N m. This nodal plane is consistent with the east-trending aftershock distribution discussed in the following section, which favors slip on the ENE-WSW (251º) nodal plane that dips steeply (70º) to the north. Since the P-axis is nearly horizontal (plunge= 4º) and trends ESE-WNW (118º), right-lateral strike-slip on an ENE-WSW trending fault is indicated. This is a surprising result since this sense of slip is inconsistent with estimates of the direction of the maximum compressive stress near the NMSZ of around 80° (Grana and Richardson, 1996), 73-84° (Ellis, 1994), or 75° (Zoback, 1992). A similar focal mechanism but with the ENE nodal plane dipping steeply south is obtained by Herrmann at St. Louis University (Herrmann, personal comm., 2003).

The preferred source depth is found by running the inversion for a range of source depths seeking the global minimum misfit. Figure 3 illustrates the changes in fitting error and source mechanism as a function of focal depth. The focal depth plotted is the depth used to generate the synthetics. For this earthquake, the fitting error reaches a minimum at 1 km depth although the focal mechanism and the fitting error for depths between 0.5 and 3 km do not vary significantly.

Aftershock Location

We deployed five portable digital seismographs with broadband seismometers within 15 hours of the mainshock (Figure 4). The early regional network location of the mainshock was very close to SUL, the first temporary station deployed. Other station locations were chosen to lie around 4 km from SUL at varying azimuths. The resulting network design was asymmetric

with respect to the aftershock locations, but not sufficiently to warrant a significant re-configuration. Station, NEAL, installed on 18 June 2003, reduced the largest azimuthal gap. OPE was moved to site OPE2 on 19 June 2003, due to potential flooding. All stations were removed on 2 July 2003. Station locations are given in Table 2.

The 3-component broadband seismometers have an instrument response that is flat to input ground velocity between 0.033 Hz and 50 Hz. At each site, seismic signals were recorded continuously at 100 samples/sec.

Over approximately four weeks, 253 seismic events were identified for the Bardwell aftershock dataset. These included local, regional, and teleseismic events and noise triggers. After event association, P- and S-wave arrival times were picked and **HYPOELLIPSE (**Lahr, 1999) was used to locate the events. We used a modified NMSZ velocity model (Chiu et al.,1992) to locate the earthquakes. This is the standard network model for locating earthquakes in the NMSZ with a modification of the top layer thickness from 600 to 340 meters. The adjustment to the soil-layer thickness was based on the soil thickness in three wells (KY18, 399 m; KY19, 249 m; KY8, 304 m) that penetrate to Paleozoic rocks in the area (Dart, 1992). The velocity model is given in Table 3.

Of the 253 identified seismic events, 85 were local aftershocks with very good signal-to-noise ratios at all stations. Initial event locations were determined with no station corrections. We defined station corrections as the average of the residuals for each station (P- and S-waves independently) for the 85 events. The station corrections are given in Table 2. These station corrections were applied when relocating the 85 aftershocks.

The aftershock locations are shown in Figure 4a as open circles. They occur directly underneath the town of Bardwell. The aftershocks define a relatively narrow east-west trend roughly 1 km in length and 0.25 km in width. The distribution of these aftershocks in the north-south cross section (open circles) shown in Figure 4b indicates a nearly vertical rupture area between 1.5 and 3.0 km depth. This is consistent with the ENE-WSW striking (strike=251°) steeply dipping (dip=70°) nodal plane of the mainshock (Figure 2).

A goal of this study is to determine the fault geometry of the mainshock from the distribution of aftershocks. However, the level of uncertainty in aftershock location is on the order of the dimension of the fault plane (see Figure 8b). The mean horizontal and vertical 68% confidence estimates are 0.4 and 1.0 km respectively. Multiple realizations of an earthquake located at the same point and having this level of uncertainty should produce an ellipsoidal cloud

with dimensions of the level of uncertainty. This suggests the actual level of uncertainty is overestimated for these events and that the locations are better than the level of uncertainty suggests.

This lead us to try a high-resolution hypocenter location algorithm. We employed the double-difference earthquake location method (Waldhauser and Ellsworth, 2000). The method incorporates travel time differences formed from P- and S-wave arrival times with differential travel times derived from waveform cross-correlation methods. It is suggested that uncertainties are improved by an order of magnitude for two basic reasons (Waldhauser and Ellsworth, 2000). First, specifying the travel time as a double difference minimizes errors due to unmodeled velocity structure. In the Mississippi embayment with deep soils, this could prove significant. Secondly, waveform cross-correlation measurements are potentially more accurate than picks made by an analyst, particularly for S-waves where the onset is often obscured by the P-wave coda.

Although Waldhauser and Ellsworth (2000) used the cross-spectral method of Poupinet et al. (1984) to measure the differential travel times, we found it unstable for signals that are not quite similar. Hence, we chose to use a cross-correlation method that we find more stable for analysis of broadband of waveforms.

The cross-correlation method used in our study is illustrated in Figure 5. In this example, the P-waves from two events at site SUL are correlated. The data are bandpass-filtered between 0.6 and 30 Hz and a 1.28-second window is applied. The windows are centered on the same specified time relative to the origin time of each event (Figure 5a). This specified time corresponds to the travel time of the phase in question for the first event. The cross-correlation of the two time series is shown in Figure 5b. The differential travel-time corresponds to the lag time of the peak in the cross-correlation function. For use in the double-difference earthquake location, only measurements having a correlation coefficient equal to or larger than 0.8 are retained, and the correlation coefficient is used to weight the uncertainty of the observations. The method has a precision of one sample (0.01 s in this study), and it is a stable estimator since non-similar signals do not satisfy the correlation coefficient threshold. Examples of correlated P- and S-wave at two stations from the same event are shown in Figure 5c.

The relocations using the double-difference method are shown as dark gray circles in Figure 4. Epicenter locations have only modest changes, and the mean of the horizontal uncertainty has been reduced from 400 to 21 meters. The distribution of epicenters still defines

an east-west trend roughly 1 km in length, which is still about 20° from the WSW–ENE striking nodal plane of the mainshock mechanism (Figure 2). A substantial compressing of the vertical distribution of hypocenters is apparent in the transverse cross-section shown in Figure 4b, and the mean of the vertical uncertainty has been reduced from 1000 to 25 meters. The hypocenters define a nearly vertical fault ranging from 2.0 to 2.7 km depth. An east-west cross-section (along strike) is shown in Figure 4c. The circular "fault plane" shown in this cross-section contains 90% of the hypocenters and has a radius of 0.44 (±0.03) km. The uncertainty in the radius is the square root of the sum of the squares of the horizontal and vertical means.

Aftershock Focal Mechanisms

Although the portable seismographic network we deployed has a limited number of stations, each station is a high quality broadband seismograph recording three components of ground motion. This enables substantial processing of the waveform data to help obtain significantly more information at each site. For each trace, instrument response is removed, horizontal components are rotated to radial- and transverse-components, and all three components are integrated to displacement after applying a high-pass filter (corner =0.4 Hz). After this processing, SH- and SV-wave polarities and the amplitude ratios of seismic phases can be determined, in addition to the P-wave first-motions. Figure 6a shows waveforms at station SUL for the example earthquake (event #4). In this case, the SV-wave polarity is clearly observed on the radial-component, and the SH-wave polarity is clearly observed on the transverse-component. While the signal-to-noise ratio was typically sufficient at station SUL to provide clear displacement waveforms, such clarity at other stations was less typical.

We employed a method to determine the double-couple earthquake focal mechanism utilizing P, SH, and SV first-motion observations, and amplitude ratios SV/SH, SH/P and SV/P to constrain the possible focal mechanisms (**FOCMEC,** Snoke et al., 1984; Snoke, 2003). Figure 6b shows the focal mechanism for the example event determined using the program FOCMEC and the larger set of constraints. We note that the focal mechanisms obtained using only the P-wave first motions at each station (e.g., **FPFIT,** Reasenberger and Oppenheimer, 1985) were unacceptable, because multiple focal mechanisms were formed to fit observed first motions.

Focal mechanisms determined for a subset of aftershocks are shown in Figure 7. Most of this subset of aftershocks occurred after installation of the station NEAL (Table 4). Although the

selection of earthquakes is somewhat arbitrary, the set still samples along the length of the fault. In general, focal mechanisms among these aftershocks are consistent with right-lateral strike-slip on a nearly vertical east-striking fault plane. The average P-axis for these events is nearly horizontal and trends ESE (~120°), which is almost identical to the mainshock P-axis orientation (see Figure 2).

Constraints on the Mainshock Location Using Waveform Cross-Correlation

The mainshock location plotted in Figure 4a as a star (Table 1) was derived from arrivals observed on the regional network and observations from the Kentucky seismographic network (Wang, 2003). It does not fall within the limits of the aftershock trend, but lies approximately 1 km to the northeast. The closest station used to locate the main shock was 13.2 km away, and 4 stations were within 20 km. However, S-wave arrivals were not estimated at those stations. The closest station having an S-arrival time was 61 km away. The distribution of seismic stations in azimuth was good. The larger of the two horizontal 68% confidence estimates is 1.2 km, and the vertical 68% confidence estimate is 1.3 km for the mainshock.

Figure 8a shows a projection of the 95% confidence ellipsoid for the mainshock onto a horizontal plane centered on its epicenter. At this level of probability, over half of the aftershocks are within the uncertainty ellipsoid for the mainshock. Figure 8b shows the projection of the 95% confidence ellipsoid for an aftershock near the center of the distribution (the aftershock uncertainty is from the original location using **HYPOELLIPSE**). At the same level of probability, the mainshock lies well outside the uncertainty ellipsoid for this event. Given the larger level of uncertainty associated with the mainshock than the aftershocks, it is likely that the true mainshock hypocenter lies within the distribution of aftershocks.

The largest aftershock on 06/08/2003 (10:51, M=2.4; Table 4) can be used to support this claim, since it was well recorded by stations of the portable network and by the regional stations that also recorded the mainshock. Figure 9 shows waveform matching for the vertical records at CCM (Cathedral Cave, Missouri, Δ=238 km) from the mainshock and the largest aftershock. Waveforms are cross-correlated with a coefficient of 0.64 suggesting that the two events are somewhat similar in their location and source radiation. Geller & Mueller (1980) and Nadeau et al. (1995) suggest using one quarter of the dominant signal wavelength as a measure location uncertainty for two well-correlated events. In this case, *Lg*-waves have a velocity of 3.5 km/s

and a dominant frequency near 2 Hz giving a quarter wavelength around 450 m. The waveform similarity suggests these two events are within 450 m (Geller & Mueller, 1980; Thorbjarnardottir and Pechmann, 1987). However, Harris (1991) reported that the correlation length can be much longer: one to two wavelengths, in some regions. The centroid of the aftershock distribution at 38.875°N and 89.010°W is our preferred mainshock location.

Discussion

Relocation of the aftershocks using the double-difference earthquake location method (Waldhauser, 2001) significantly reduced the location uncertainty while leaving the east-west trend in epicenters largely unchanged. The distribution of aftershocks in a north-south cross-section is consistent with a nearly vertical east-striking fault at depths between 2.0 to 2.7 km. For the east-west cross-section (along strike), a circular "fault plane" containing 90% of the hypocenters has a radius of about 0.44 (±0.03) km.

The east-west trending 1 km long rupture area inferred from the aftershock distribution suggests that the west-southwest striking nodal plane (strike=251º) of the mainshock focal mechanism is likely the fault plane, although there is about 20º discrepancy between the strike of the mainshock mechanism and the EW trend of the aftershock lineation. The range of uncertainty for the strike, dip and rake of the mainshock source mechanism are estimated to be 4º, 6º, and 7º, respectively (see Du et al., 2003) and hence, it is difficult to reconcile this difference.

One of the main values of this aftershock deployment is that the constraints placed upon the faulting geometry of the main shock by the distribution of aftershocks allow inferences regarding source scaling. The fault radius can be used along with the seismic moment obtained from the waveform inversion to determine the static stress drop, $\Delta\sigma$, of the mainshock. The relationship between static stress drop, seismic moment (M_0), and fault radius (r) is given by $\Delta\sigma = 7/16\ M_0/r^3$ (Keilis-Borok, 1959; Kanamori & Andersion, 1975). For the seismic moment, $M_0 = 1.3 \times 10^{15}$ N m, the mainshock has a static stress drop $\Delta\sigma = 67\ (\pm 14)$ bars where the uncertainty is related entirely to the uncertainty in fault radius. Atkinson and Hanks (1995) based on fits to high frequency ground motion observations suggest that the average stress drop for earthquakes in eastern North America is 150 bars. However, the variability between earthquakes is substantial and 67 bars is not unusual.

While earthquakes in the NMSZ generally concentrate in the Precambrian basement over the depth range of 4-14 km (Chiu et al. 1992; Pujol et al. 1997), the Bardwell aftershocks are concentrated between depths of 2.0 to 2.7 km consistent with estimates of the focal depth of the mainshock. The Mw=3.6 event of 08/14/1965 (Table 1; Figure 11) also has a shallow source depth of 1.5 km (Herrmann, 1979; Nuttli, 1982). These events nucleate and propagate entirely within Paleozoic sedimentary rocks, since the top of the Precambrian basement is between 3 and 4 km deep in this area (McBride et al., 2003). Rupture that nucleates within the Paleozoic rocks indicates that these rocks store potential strain energy. A search of the Center for Earthquake Research and Information (CERI), University of Memphis catalog for events in the immediate area since 1992 produces

- the m=2.1 Lovelaceville, KY with depth of 9.1 km (1993/01/11),
- the m=2.6 Blandville, KY with depth of 8.2 km (1993/07/29),
- the m=3.4 Blandville, KY with depth of 12.7 km (1994/09/26).

showing that earthquakes occur over a normal depth range in the study area.

The focal mechanism of the mainshock determined from regional waveform inversion (Figure 2) as well as the mechanisms for ten aftershocks determined from P- and S-wave polarities and amplitude ratios (Figure 7) are all consistent with a strike-slip stress regime, with the average P-axis orientation trending 120°. The axes of a focal mechanism represent principal strains rather than principal stresses, and the two are not generally coincident. McKenzie (1969) states that for the general case of triaxial stress, the only restriction is that the greatest principal stress direction must lie in the quadrant containing the P axis. Given the east trending fault indicated by the aftershock distribution (Figure 4), the underlying maximum compressive stress (σ_1) direction for the Bardwell earthquakes must lie between 90°-180°.

To assess the state of stress around the Bardwell area, we invert the focal mechanisms of the aftershocks for the local stress tensor (Gephart, 1990). The results of the stress inversion indicate that the local σ_1 trends 104° with a plunge of 5° (Figure 10). The intermediate stress axis (σ_2) is nearly vertical indicating a strike-slip stress regime (Gephart and Forsyth, 1984).

Zoback and Zoback (1991) find the direction of σ_1 measured throughout North America is remarkably consistent with the orientation of the plate-driving forces associated with the ridge-push force. For eastern North America as a whole, the mean σ_1 direction is estimated to be about 60° -65°. The local stress field near Bardwell is therefore rotated around 40° clockwise relative to ENA. Others have observed a smaller σ_1 clockwise rotation for the NMSZ area of 80° (Grana

and Richardson, 1996), 73-84° (Ellis, 1994) or 75° (Zoback, 1992). On an east-striking fault, these estimates would have produced left lateral strike-slip motion, rather than the right lateral observed for the Bardwell sequence of earthquakes.

It is interesting to compare the focal mechanism of the Bardwell event to other similar size events in the region (Table 1; Figure 11). The focal mechanisms with red fill and the one with blue fill have the opposite sense of motion for the east trending plane. Since the σ_1 direction must lie in the quadrant containing the P axis (McKenzie, 1969), this requires a rotation of the stress field where the σ_1 lies in the northeast quadrant for the region with red-fill earthquakes but in the southeast quadrant for the blue-fill Bardwell event. The implication is that a strong perturbation in the stress field occurs between Bardwell, KY and New Madrid, MO a distance of about 60 km. Further, the stress field near New Madrid appears to deviate less with respect to that of ENA than the stress field near Bardwell.

It is notable that under the constraint that the σ_1 direction must lie in the quadrant containing the P axis both the red and blue fill mechanisms are generally compatible with the black fill while not being compatible with each other. An exception is the October 1965 earthquake in the Ozark Uplift that had a dip-slip focal mechanism. The rotation of stress field over a distance of 60 km between New Madrid and Bardwell may indicate a local source of stress in the crust. Potential sources of localized stress rotation in the NMSZ include static stress changes created by 1811-1812 earthquakes, local flexure due to sediment load, and buoyancy forces related to the "Rift pillow," although the latter would seemingly rotate the stress field for the red-fill earthquakes as well.

Conclusions

Detailed analysis of regional and local waveform data from the 6 June 2003 Bardwell, Kentucky, earthquake sequence indicates that the Mw 4 mainshock occurred at a depth of about 2 (±1) km. The source mechanism determined from regional waveform analysis shows predominantly strike-slip faulting along near-vertical nodal planes with a near horizontal P axis (plunge= 4º and trend= 118º).

Following the mainshock, 85 aftershocks were recorded during four weeks of local network deployment. Locations of the aftershocks obtained using a high-resolution technique (double-difference method), delineate an east-west trending 1 km long rupture area (Figure 4).

In a transverse (-) cross-section, the aftershocks illuminate a nearly vertical plane between 2.0 and 2.7 km depth in general agreement with the west-southwest striking nodal plane (dip=70º and strike=251º) of the mainshock focal mechanism (cf. Figures 2 & 4).

The aftershock cluster in the along-strike cross-section is interpreted as a circular fault area with a radius of about 0.44 (±0.03) km. This source radius yields a static stress drop, $\Delta\sigma$ = 67 (±14) bars for the mainshock with a seismic moment, $M_0 = 1.3 \times 10^{15}$ N m.

A formal stress inversion based on the focal mechanisms of the mainshock and ten aftershocks indicates the maximum compressive stress trends 104° with a plunge of 5°. The local stress field near Bardwell is therefore rotated around 40° clockwise relative to eastern North America as a whole. The Bardwell earthquakes have the opposite sense of slip to earthquakes that occur near New Madrid, MO. This requires a large rotation of stress field over a distance of 60 km providing evidence for a local source of stress in the crust.

Acknowledgments

We would like to thank John Filipcic at CERI, Univ. of Memphis for assisting with the aftershock survey. We are grateful to Arch Johnston at CERI, Paul Richards and Jim Gaherty at LDEO for their critical review and valuable comments. Zeming Wang at Kentucky Geological Survey kindly provided waveform data from the Kentucky Network stations. This research work is sponsored by the U.S. Geological Survey under Grant Number 01-HQ-AG-0137 (PI, W.Y. Kim, LDEO). This is CERI contribution number 479 and Lamont-Doherty Earth Observatory contribution number xxxx.

References

Atkinson, G. M., and T. C. Hanks (1995). A high-frequency magnitude scale, *Bull. Seism. Soc. Am.*, 85, 825-833.

Bickford, M. E., W. R. Van Schums, and I. Zietz (1986). Proterozoic history of the mid-continent region of North America, *Geology*, **14**, 492-496.

Burke, K. and Dewey, J.F., 1973, Plume-generated triple junctions; key indicators in applying plate tectonics to old rocks, *J. Geol*. **81**,406-433.

Chiu, J. M., A. C. Johnston, and Y. T. Yang (1992). Imaging the active faults of the central New Madrid seismic zone using PANDA array data, *Seism. Res. Letters* **63**, 375-393.

Dart, R. L. (1992). Catalog of pre-Cretaceous geologic drill-hole data from the upper Mississippi embayment: a revision and update of open-file report 90-260, *U. S. Geological Survey Open-File Report 92-685*.

Du, Wen-xuan, Won-Young Kim, and Lynn R. Sykes (2003). Earthquake source parameters and state of stress for northeastern United States and southeastern Canada from analysis of regional seismograms, *Bull. Seism. Soc. Am.*, **93**, 1633-1648.

Ellis, W. L. (1994). Summary and discussion of crustal stress data in the region of the New Madrid seismic zone, *U. S. Geological Survey Open-File Report 1538-B.*

Ervin, C.P., and L.D. McGinnis (1975). Reelfoot rift: Reactivated pre- cursor to the Mississippi embayment, *Geol. Soc. Am. Bull,* **86**, 1,287-1,295

Geller, R.J. and C.S. Mueller (1980). Four similar earthquakes in central California, *Geophys. Res. Lett*., **7**, 821-824.

Gephart, J. W. (1990). **FMSI**: a FORTRAN program for inverting fault/slikenside and earthquake focal mechanism data to obtain the regional stress tensor, *Computers & Geosciences* **16**, 953-989.

Gephart, J. W., and D. W. Forsyth (1984). An improved method for determining the regional stress tensor using earthquake focal mechanism data: Application to the San Fernando earthquake sequence, *J. Geophys. Res.*, **89**, 9305-9320.

Grana, J. P. and R. Richardson (1996). Tectonic stress within the New Madrid seismic zone, *J. Geophys. Res.* **101**, no. B3, 5445-5458.

Ginzburg, A., W. D. Mooney, A. W. Walter, W. J. Lutter and J. H. Healy (1983). Deep structure of the northern Mississippi embayment, *AAPG Bull*. **67**, 20031-2046.

Gordon, D. (1988). Revised instrumental hypocenters and correlation of earthquake locations and tectonics in the central United States, *U.S. Geological Survey Professional Paper 1364*, 69 pp.

Harris, D.B. (1991). A waveform correlation method for identifying quarry explosions, *Bull. Seism. Soc. Am.*, ***81***, 2395-2418.

Herrmann, R. B. (1979). Surface wave focal mechanisms for eastern North America with tectonic implications, *J. Geophys. Res.*, **84**, 3543-3552.

Herrmann, R. B. (2003)

Hildenbrand, T.G., M.F. Kane, and W Stauder (1977). Magnetic and gravity anomalies in the northern Mississippi embayment and their spatial relation to seismicity, *US. Geol. Surv. Misc. Field Studies Map MF-914,* scale 1:1,000,000.

Hildenbrand, T.G., M.F. Kane, and J.D. Hendricks (1982). Magnetic basement in the upper Mississippi embayment region-a preliminary report, in McKeown, F.A., and L.C. Pakiser, eds., Investigations of the New Madrid, Missouri, Earthquake Region, *US. Geol. Surv. Prof Paper* 1236, 39-53.

Hildenbrand, T.G. (1985). Rift structure of the northern Mississippi embayment from the analysis of gravity and magnetic data: *J. Geophys. Res.*, **90**, 12,607- 12,622.

Howe, J.R. (1984). Tectonics, sedimentation and hydrocarbon potential of the Reelfoot aulacogen. M.S. thesis, University of Oklahoma, Norman, OK, 75 pp.

Kanamori, H. and D.L. Andersion (1975). Theoretical basis of some empirical relations in seismology, *Bull. Seism. Soc. Am.,* **65**, 1073-1095.

Kane, M.F., T.G. Hildenbrand, and J.D. Hendricks, (1981). Model for the tectonic evolution of the Mississippi embayment and its contemporary seismicity, *Geology* **9**,563-568.

Keilis-Borok, V. (1959). On estimation of the displacement in an earthquake source and of source dimension, *Ann. Geofis*., **12**, 205-214.

Kim, Won-Young (2003). 18 June 2002 Caborn, Indiana Earthquake: Reactivation of Ancient Rift in the Wabash Valley Seismic Zone?, *Bull. Seism. Soc. Am.*, **93**, 2201-2211.

Kolata, D. R., J. D. Treworgy, and J. M. Masters (1981). Structural framework of the Mississippi embayment of southern Illinois, *Illinois State Geol. Surv. Circular* 516, 38p.

Kolata, D. R., and W. J. Nelson (1991). Tectonic history of the Illinois Basin, M. S. Leighton, D. R. Kolata, D. F. Oltz, and J. J. Eidel (Editors), *Am. Assoc. Petrol. Memoir*, vol. **51**, 263-285.

Lahr, J. C, (1999). HYPOELLIPSE: A computer program for determining local earthquake hypocentral parameters, magnitude, and first-motion pattern, *U. S. Geological Survey Open-File Report 99-23*.

Langer, C.J. And G.A. Bollinger (1991), The southeastern Illinois earthquake of 10 June 1987: The later aftershocks, *Bull. Seism. Soc. Am.*, **81**, 423-445.

Langston, C.A. (1994). An integrated study of crustal structure and regional wave propagation for southern Missouri, *Bull. Seism. Soc. Am.*, **84**, 105-118.

McBride, J. H., D. R. Kolata, and T. G. Hildenbrand (2003). Geophysical constraints on understanding the origin of the Illinois basin and its underlying crust, *Tectonophysics*, **363**, 45-78.

McKenzie, D. P. (1969). The relation between fault plane solutions for earthquakes and the directions of the principal stresses, *Bull. Seism. Soc. Am.* 59,591-601.

Mooney, W. D., M. C. Andrews, A. Ginzburg, D. A. Peters and R. M. Hamilton (1983). Crustal structure of the northen Mississippi embayment and comparison with other continental rift zones, *Tectonophysics* **94**, 327-348.

Munson, P.J., S.F. Obermeier, C.A. Munson, and E.R. Hajic (1997). Liquefaction evidence for Holocene and latest Pleistocene seismicity in the southern halves of Indiana and Illinois: A preliminary overview, *Seism. Res. Left.*, **68**, 521-536.

Nadeau, R.M., W. Foxall, and T.V. McEvilly (1995). Clustering and periodic recurrence of microearthquakes on the San Andreas fault at Parkfield, California, *Science*, **267**, 503-507.

Newman, A., S. Stein, J. Weber, J. Engeln, A. Mao, and T. Dixon (1999). Slow deformation and lower seismic hazard at the New Madrid seismic zone, *Science*, **284**, 619-621.

Nuttli, O.W. (1982), Damaging earthquakes of the Central Mississippi Valley, *U.S. Geol. Survey Professional Paper 1236-B*, 15-20.

Poupinet, G., W.L. Ellsworth and J. Frechet (1984). Monitoring velocity variations in the crust using earthquake doublets: an application to the Calaveras fault, California, *J. Geophys. Res.* **89**, no. B7, 5719-5731.

Pujol, J., A. C. Johnston, J.M. Chiu, and Y. T. Yang (1997). Refinement of thrust faulting models for the central New Madrid seismic zone, *Engineering Geology* **46**, 281-298.

Reasenberg, P.A. and D. Oppenheimer (1985). **FPFIT**, FPPLOT and FPPAGE: Fortran computer programs for calculating and displaying earthquake fault-plane solutions. *U.S. Geological Survey Open-File Report 85-739*.

Saikia, C. K. (1994). Modified frequency-wavenumber algorithm for regional seismograms using Filon's quadrature: modeling of Lg waves in eastern North America, *Geophys. J. Int.*, **118**, 142-158.

Santillan, V.M., R. Smalley, Jr.M. Ellis (2002). Deformation in the New Madrid Seismic Zone from continuous GPS Geodesy, AGU meeting at San Francisco, California

Snoke, J. A. (2003). **FOCMEC**: Focal mechanism determinations, URL: http://www.geol.vt.edu/outreach/vtso/focmec/.

Snoke, J. A., J. W. Munsey, A. C. Teague, and G. A. Bollinger (1984). A program for focal mechanism determination by combined use of polarity of SV-P amplitude ratio data, *Earthquake Notes* **55**, no. 3, 15.

Soderberg, R.K., and G.R. Keller (1981). Geophysical evidence for deep basin in western Kentucky, *Am. Assoc. Pet. Ceol. Bull*, **65**, 226-234.

Stauder, W. and O.W. Nuttli (1970), Seismic studies: South central Illinois earthquake of November 8, 1968, *Bull. Seism. Soc. Am.*, **60**, 979-981.

Stearns, R. (1957). Cretaceous, Paleocene, and lower Eocene geologic history of the northern Mississippi embayment, *Bull. Geol. Soc. Am.* **68**, 1077-1100.

Taylor, K.B., R.B. Herrmann, M.W. Hamburger, G.L. Pavlis, A. Johnston, C.J. Langer, and C. Lam (1989), The southeastern Illinois earthquake of 10 June 1987, *Seism. Res. Lett.*, **60**, 101-110.

Thorbjarnardottir, B.S. and J. Pechmann (1987). Constraint on relative earthquake locations from cross-correlation of waveforms, *Bull. Seism. Soc. Am.*, ***77***, 21626-1634.

Tio, H. K., and H. Kanamori (1995). Moment tensor inversion for local earthquakes using surface waves recorded at TERRAscope, *Bull. Seism. Soc. Am.*, ***85***, 1021-1038.

Tuttle, M. P., E. S. Schweig, J. D. Sims, R. H. Lafferty, L. W. Wolf, and M. L. Haynes (2002). The earthquake potential of the New Madrid seismic zone, *Bull. Seism. Soc. Am* **92**, 2080-2089.

Waldhauser, F. and W. L. Ellsworth (2000). A double-difference earthquake location algorithm: method and application to the northern Hayward fault, California, *Bull. Seism. Soc. Am.* **90**, no. 6, 1353-1368.

Waldhauser, F. (2001). **HypoDD** - - A program to compute double-difference hypocenter locations, *U. S. Geological Survey Open-File Report 01-113*.

Wang, Z., E. W. Woolery, and B. Shi (2003). Observed seismicity (earthquake activity) in the Jackson Purchase region of western Kentucky: January through June 2003, Special Publication 6, Kentucky Geological Survey, Series XII.

Wheeler, R. L. (1997). Boundary separating the seismically active Reelfoot rift from the sparsely seismic Rough Creek graben, Kentucky and Illinois, *Seism. Res. Letters* **68**, 586-598.

Yang, J. and Y. P. Aggarwal (1981). Seismotectonics of northeastern United States and adjacent Canada, *J. Geophys. Res.*, **86**, 4981-4998.

Zhao, L. S., and D. V. Helmberger (1994). Source estimation from broadband regional seismograms, *Bull. Seism. Soc. Am.*, ***84***, 91-104.

Zoback, M.D., and Zoback, M.L., 1991, Tectonic stress field of North America and relative plate motions, *in* Slemmons, D.L., Engdahl, E.R., Zoback, M.D., and Blackwell, M.D., eds., Neotectonics of North America: Boulder, Colorado, Geological Society of America, p. 339-366.

Zoback, M. L. (1992). Stress field constraints on intraplate seismicity in Eastern North America, *J. Geophys. Res.*, **97**, B8, 11761-11782.

Authors Affiliations
Stephen Horton and Mitch Withers
3876 Central Avenue
Center for Earthquake Research and Information,
University of Memphis
Memphis, TN 38152

E-mail: shorton@memphis.edu
Phone: 901-678-4896
Fax: 901-678-4734

Won-Young Kim
Lamont-Doherty Earth Observatory
of Columbia University,
61 Route 9W,
Palisades, NY 10964,
USA.

E-mail: wykim@ldeo.columbia.edu
Phone: 845-365-8387
FAX: 845-365-8150

Table 1. 2003 Bardwell, Kentucky, Earthquake and other Significant Earthquakes in the region

Date (year-mo-dy)	Origin time (hh:mm:sec)	Lat. (°N)	Long. (°W)	Depth (km)	Magnitude* (mb)	(M_W)	P axis (trend/plunge)	Reference
2003-06-06	12:29:34	36.878	88.996	2.5	4.5		CERI	
2003-06-06	12:29:34	36.875	89.010	2.0	4.5	4.0	118/04	this study
			New Madrid seismic zone					
1962-02-02	06:43:34	36.5	89.6	7.5	4.3	4.2	043/19	1
1965-08-14	13:13:56	37.2	89.3	1.5	3.8	3.6	239/28	1,8
1968-03-03	17:30:11	36.7	90.1	15	4.8	4.7	174/11	1
1970-11-17	02:13:55	35.9	89.9	16	4.4	4.1	272/09	1
1975-06-13	22:40:27	36.54	89.68	9	4.2	3.7	049/34	1
1976-03-25	00:41:20	35.59	90.48	16	5.0	4.6	272/01	1,8
1976-03-25	01:00:12	35.61	90.48	16	4.5	4.2	271/28	1,8
1990-09-26	13:18:51	37.170	89.577	12	4.7	4.3	280/05	6
1991-05-04	01:18:55	36.56	89.83	5	4.6	4.3	040/04	6
1994-02-05	14:55:37	37.368	89.188	16	4.2			??
			Illinois basin and Wabash Valley seismic zone					
1968-11-09	17:01:42	37.95	88.48	25	5.5	5.3	097/01	1,2, 3, 8
1974-04-03	23:05:03	38.6	88.1	15	4.7	4.4	267/14	1
1987-06-10	23:48:55	38.71	87.95	10	4.9	5.0	086/00	4, 5
2002-06-18	17:37:17	37.992	87.772	18	5.0	4.6	252/10	7
			Ozark Uplift					
1965-10-21	02:04:38	37.5	91.0	5	4.9	4.6	273/76	1
1967-07-21	09:14:49	37.5	90.4	15	4.3	4.0	314/52	1
1998-01-05								??

* Magnitude: mb= mb(Lg), 1-sec period Lg-wave magnitude, M_W = Moment magnitude,
Reference: (1) Herrmann, 1979; (2) Stauder & Nuttli, 1970; (3) Gordon, 1988; (4) Taylor et al., 1989; (5) Langer & Bollinger, 1991, (6) Langston, 1994; (7) Kim, 2003; (8) Nuttli, 1982.

Table 2. Station Information for Bardwell Aftershock Network.

Station code	Latitude (°N)	Longitude (°W)	Elevation (meters)	P-correction (seconds)	S-correction (seconds)
SUL	36.88848	89.01125	109	0.00	-0.05
LTB	36.89849	88.96704	102	0.00	0.16
HUNT	36.89412	89.06062	117	0.01	0.11
OPE	36.92128	89.00458	98	-0.01	0.07
OPE2	36.90718	89.00941	105	0.00	0.03
CHIE	36.84871	88.99847	136	0.00	-0.06
NEAL	36.85692	89.04115	132	0.01	0.06

Table 3. Modified New Madrid Velocity Model

Layer no.	Thickness (km)	V_P (km/s)	V_S (km/s)
1	0.34	1.80	0.60
2	2.16	6.02	3.56
3	2.5	4.83	3.20
4	12.0	6.17	3.57
5	10.0	6.60	3.82
6		7.30	4.22

Table 4. Mainshock and large aftershocks (*)

Event Id	Date Mo/Dy/Year	Time hh:mm:sec	Lat. (°N)	Long. (°W)	Depth (km)	Magnitude (M_L)
main	06/06/2003	12:29:34.0	36.875	89.010	2.0	4.5
1	06/07/2003	11:07:00.18	36.8743	89.0085	2.08	1.9
	06/08/2003	01:02:14.70	36.8740	89.0040	1.70	2.0
2	06/08/2003	10:51:38.80	36.8750	89.0058	2.13	2.4
	06/09/2003	07:32:28.85	36.8748	89.0060	2.78	2.2
	06/10/2003	07:41:33.26	36.8743	89.0065	2.05	2.1
	06/12/2003	20:05:27.85	36.8743	89.0065	2.09	2.1
	06/12/2003	22:51:39.54	36.8750	89.0068	3.10	2.1
3	06/21/2003	07:47:51.61	36.87417	89.00450	2.53	1.6
4	06/23/2003	04:13:08.83	36.87483	89.00484	2.54	1.7
5	06/23/2003	06:15:23.63	36.87417	89.01017	2.52	1.3
6	06/24/2003	12:21:43.52	36.87400	89.00850	0.99	1.4
7	06/25/2003	01:21:02.63	36.87433	89.00750	2.18	1.5
8	06/27/2003	05:40:32.25	36.87500	89.00484	2.53	1.7
9	07/02/2003	10:36:31.50	36.87417	89.00684	2.76	1.9
10	07/02/2003	10:37:20.21	36.87400	89.00767	2.86	1.3

(*) Events identified by its id are those aftershocks used to determine focal mechanisms plotted in Figure 7. Event #2 is the largest aftershock which was used as the master event to re-locate mainshock using regional waveform data.

Figure Captions

Figure 1. Major geologic features around the epicentral area – the Mississippi embayment and Illinois basin are indicated as shaded areas. The epicenter of the 6 June 2003 Bardwell, Kentucky, earthquake is plotted with a *star*. Heavy dashed lines indicate the Reelfoot rift, a failed rift system in the northern Mississippi embayment. The Rough Creek graben in western Kentucky and the Rough Creek fault, as well as Wabash Valley fault system (WVFS) along southeastern Illinois-southwestern Indiana border are indicated by solid lines with tics on downthrown sides. Earthquakes with $mb_{Lg} \geq 2.5$ in the New Madrid seismic zone (NMSZ) and events with $mb_{Lg} \geq 4.5$ that occurred in other areas during 1960-2002 are plotted for reference (Central Mississippi Valley Earthquake catalog, 1975-1994, St. Louis University; Gordon, 1988 and PDE monthly listing). Modern broadband seismographic stations are plotted with *solid triangles* and source-receiver paths are indicated by dotted lines.

Figure 2. Comparison between observed (*gray lines*) and synthetic (*black lines*) waveforms of the 6 June 2003 earthquake. Synthetic seismograms are calculated for a focal depth of 1 km. Station code and component (Z=vertical, R=radial, T=transverse components), peak amplitude of the observed signal in micrometers, seismic moment in 10^{15} N m and time shift dt in seconds are indicated at the end of each trace. Focal mechanism of the event is represented by the typical beach ball representation of lower-hemisphere projection. Shaded quadrants denote compression for *P* waves. The epicentral distance of each station is marked around the beach ball according to azimuth. For those stations whose *P*-wave polarity data are used, a circle is plotted for compressional first motion and a triangle is used for dilatational first motion. Two nodal planes (NP1 and NP2), as well as azimuth and plunge angle in degrees of the *P* and *T* axes are indicated. The simple triangular source time function used is shown.

Figure 3. Changes of the fitting error (*E*) and source mechanism as a function of focal depths for the 6 June 2003 Bardwell, Kentucky earthquake. The fitting error reaches a global minimum (*Emin*) at 1 km depth. The inversion results for focal depths between 0.5 and 3 km produce similar overall waveform fits, as well as, source mechanisms indicating a range of acceptable depths. Acceptable results fall below the horizontal dashed line representing 5% greater fitting error, $1.05 \times Emin$.

Figure 4. a). Broadband seismometers (*black squares*) deployed following the Bardwell earthquake. SUL is located at the initial estimate of the mainshock epicenter. The star gives the current estimate based on the regional network. Initial aftershock epicenters (*open circles*) and relocated epicenters (*dark circles*) clearly delineate an east trending zone approximately 1 km in length; b). North-south cross section shows aftershocks are consistent with a vertical east trending fault. The relocated hypocenters (*dark circles*) are more concentrated in the vertical dimension, and they are still consistent with a vertical fault, c). A circle of radius 0.44 km including 90% of the relocated aftershocks is displayed in this east-west cross section

Figure 5. a) *P*-wave window for two events plotted relative to the adjusted arrival time (see text), b) Normalized cross-correlation showing optimum lag time (differential travel time), c) Examples of *P*-waves and *S*-waves at two stations after adjustment by lag time.

Figure 6. a) Displacement waveforms at station SUL for event #4. Horizontal waveforms are rotated to radial and transverse allowing identification of S wave polarity. B) Focal mechanism for event #4.

Figure 7. Aftershock focal mechanisms inferred from P- and S-wave polarities and ratios using the program **FOCMEC**. Event id is listed in Table 4.

Figure 8. a) Projection onto a horizontal plane of the 95% confidence ellipsoid for the mainshock location. Note that many aftershocks occur outside of the specified confidence area. b). Projection onto a horizontal plane of the 95% confidence ellipsoid for an aftershock near the center of the distribution. Note that the mainshock location (*star*) is clearly outside the specified confidence area for this event.

Figure 9. (*upper panel*) Regional EW-component records at CCM (Δ=238 km, AZ=304°) from the mainshock (*red trace*) and the largest aftershock on 06/08/2003 10:51 (M=2.4)(*blue trace*). Traces are plotted aligned to their *P*-wave travel times, (*lower panel*) Two traces are superposed after the waveform cross-correlation. Notice that cross-correlation is performed for 35 seconds time window, and the waveforms appears to be correlated to their largest amplitude arrivals (i.e., *Lg* arrivals) with correlation coefficient 0.64 and time lag of 0.187s, whereas the *P* waves are misaligned. Due to poor signal-to-noise ratio of *P* window for the aftershock, differential *S-P* times could not be determined, which could put constraint on the mainshock location relative to the master event.

Figure 10. Maximum principal stress axis, σ_1 (*square*), intermediate axis, σ_2 (*triangle*), and least principal stress axis, σ_3 (*circle*) determined from inverting the focal mechanisms from 10 aftershocks. Notice that the orientation of the σ_1 is consistent with the *P* axis direction (118° or 298°) of the mainshock focal mechanism shown in Figure 2.

Figure 11. Focal mechanisms of the earthquakes that occurred in central U.S. since 1960s are plotted with color-coded beach balls (lower hemisphere projection of nodal planes). Solid lines show major geologic features around epicentral area with teeth on the downthrown side. These are from the south; the Reelfoot rift, a failed rift system in the northern Mississippi embayment, Rough Creek graben in western Kentucky, and the Wabash Valley fault system (WVFS) along southeastern Illinois-southwestern Indiana border. Tertiary limit that outlines the Mississippi embayment is indicated by *heavy solid line*. Earthquakes (*gray circles*) defining the New Madrid seismic zone (NMSZ) are shown to give the geometric orientation with the study area. The 6 June 2003 Bardwell, Kentucky earthquake is indicated by a *blue beach ball*. Focal mechanisms of earthquakes in the NMSZ with east-west trending nodal plane that have NE-ENE trending *P* axis are plotted by *red beach balls*. A comparison between Bardwell and New Madrid events, hence, indicates a strong perturbation in the stress field over a distance of about 60 km.

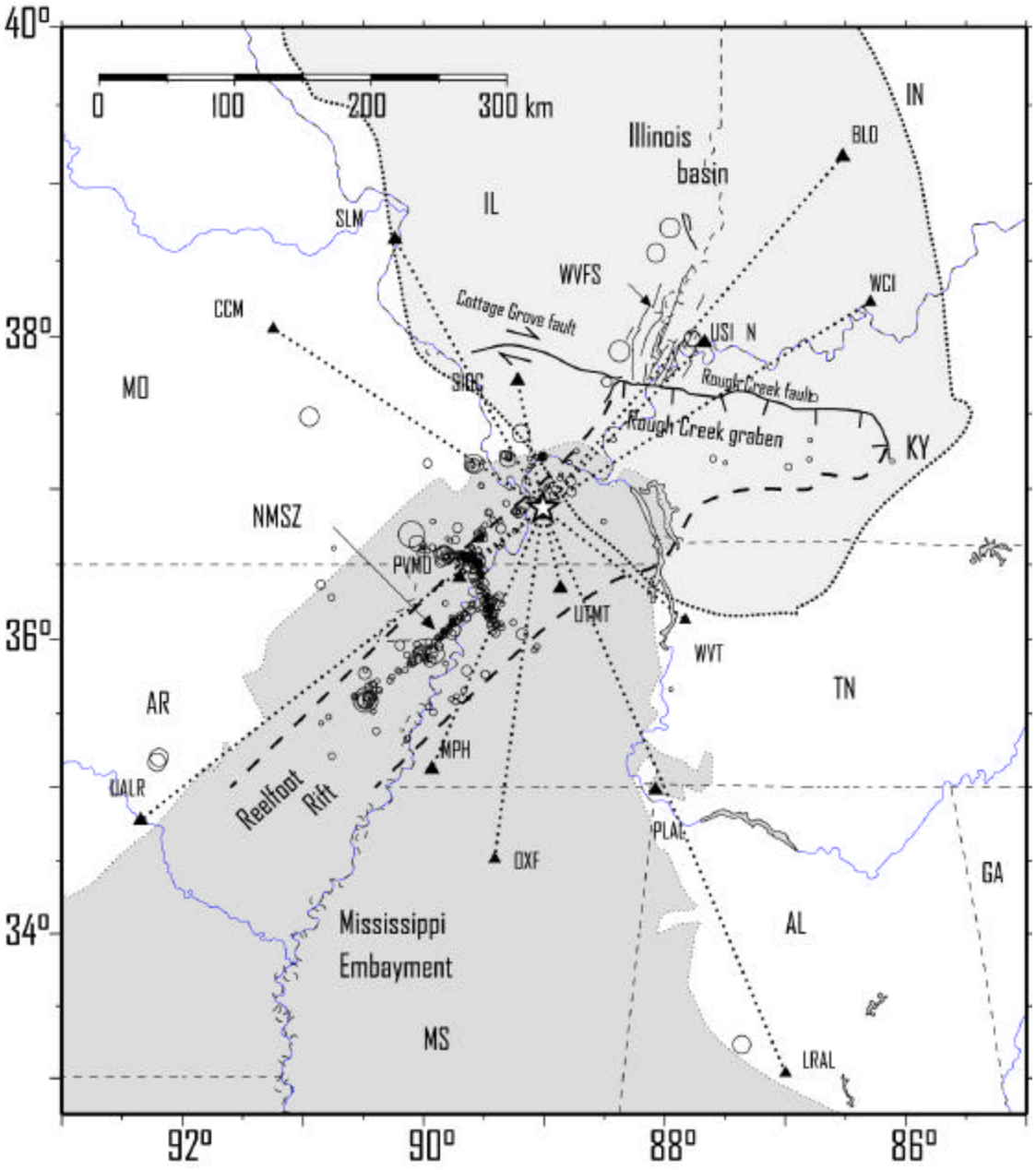

Figure 1. Major geologic features around the epicentral area – the Mississippi embayment and Illinois basin are indicated as shaded areas. The epicenter of the 6 June 2003 Bardwell, Kentucky, earthquake is plotted with a *star*. Heavy dashed lines indicate the Reelfoot rift, a failed rift system in the northern Mississippi embayment. The Rough Creek graben in western Kentucky and the Rough Creek fault, as well as Wabash Valley fault system (WVFS) along southeastern Illinois-southwestern Indiana border are indicated by solid lines with tics on downthrown sides. Earthquakes with $mb_{Lg} \geq 2.5$ in the New Madrid seismic zone (NMSZ) and events with $mb_{Lg} \geq 4.5$ that occurred in other areas during 1960-2002 are plotted for reference (Central Mississippi Valley Earthquake catalog, 1975-1994, St. Louis University; Gordon, 1988 and PDE monthly listing). Modern broadband seismographic stations are plotted with *solid triangles* and source-receiver paths are indicated by dotted lines.

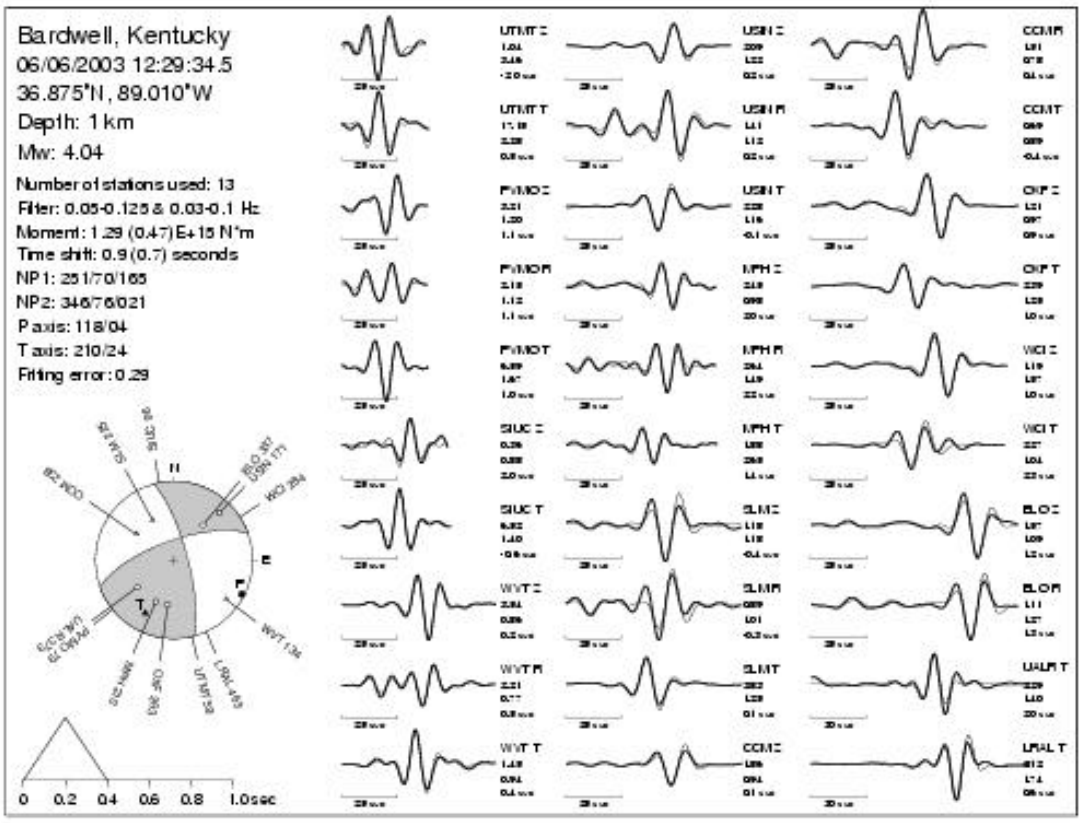

Figure 2. Comparison between observed (*gray lines*) and synthetic (*black lines*) waveforms of the 6 June 2003 earthquake. Synthetic seismograms are calculated for a focal depth of 1 km. Station code and component (Z=vertical, R=radial, T=transverse components), peak amplitude of the observed signal in micrometers, seismic moment in 10^{15} N m and time shift dt in seconds are indicated at the end of each trace. Focal mechanism of the event is represented by the typical beach ball representation of lower-hemisphere projection. Shaded quadrants denote compression for *P* waves. The epicentral distance of each station is marked around the beach ball according to azimuth. For those stations whose *P*-wave polarity data are used, a circle is plotted for compressional first motion and a triangle is used for dilatational first motion. Two nodal planes (NP1 and NP2), as well as azimuth and plunge angle in degrees of the *P* and *T* axes are indicated. The simple triangular source time function used is shown.

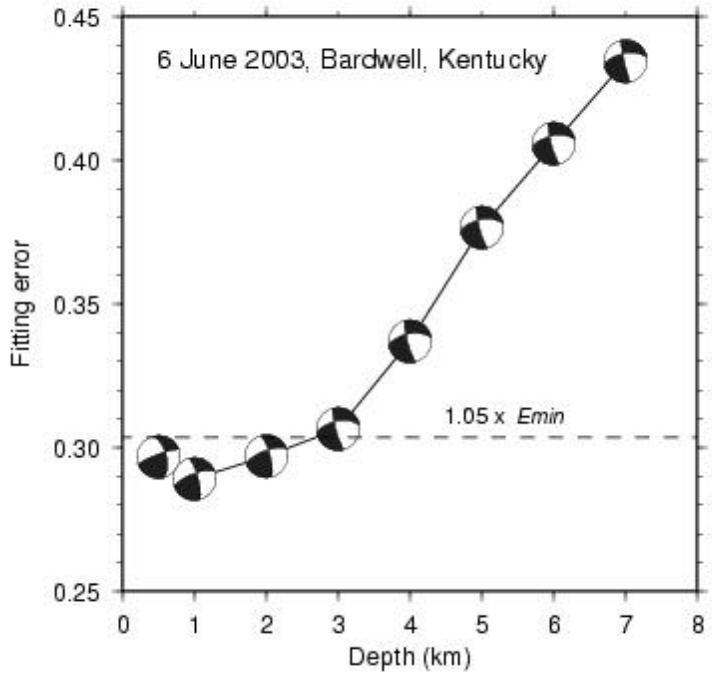

Figure 3. Changes of the fitting error (*E*) and source mechanism as a function of focal depths for the 6 June 2003 Bardwell, Kentucky earthquake. The fitting error reaches a global minimum (*Emin*) at 1 km depth. The inversion results for focal depths between 0.5 and 3 km produce similar overall waveform fits, as well as, source mechanisms indicating a range of acceptable depths. Acceptable results fall below the horizontal dashed line representing 5% greater fitting error, $1.05 \times Emin$.

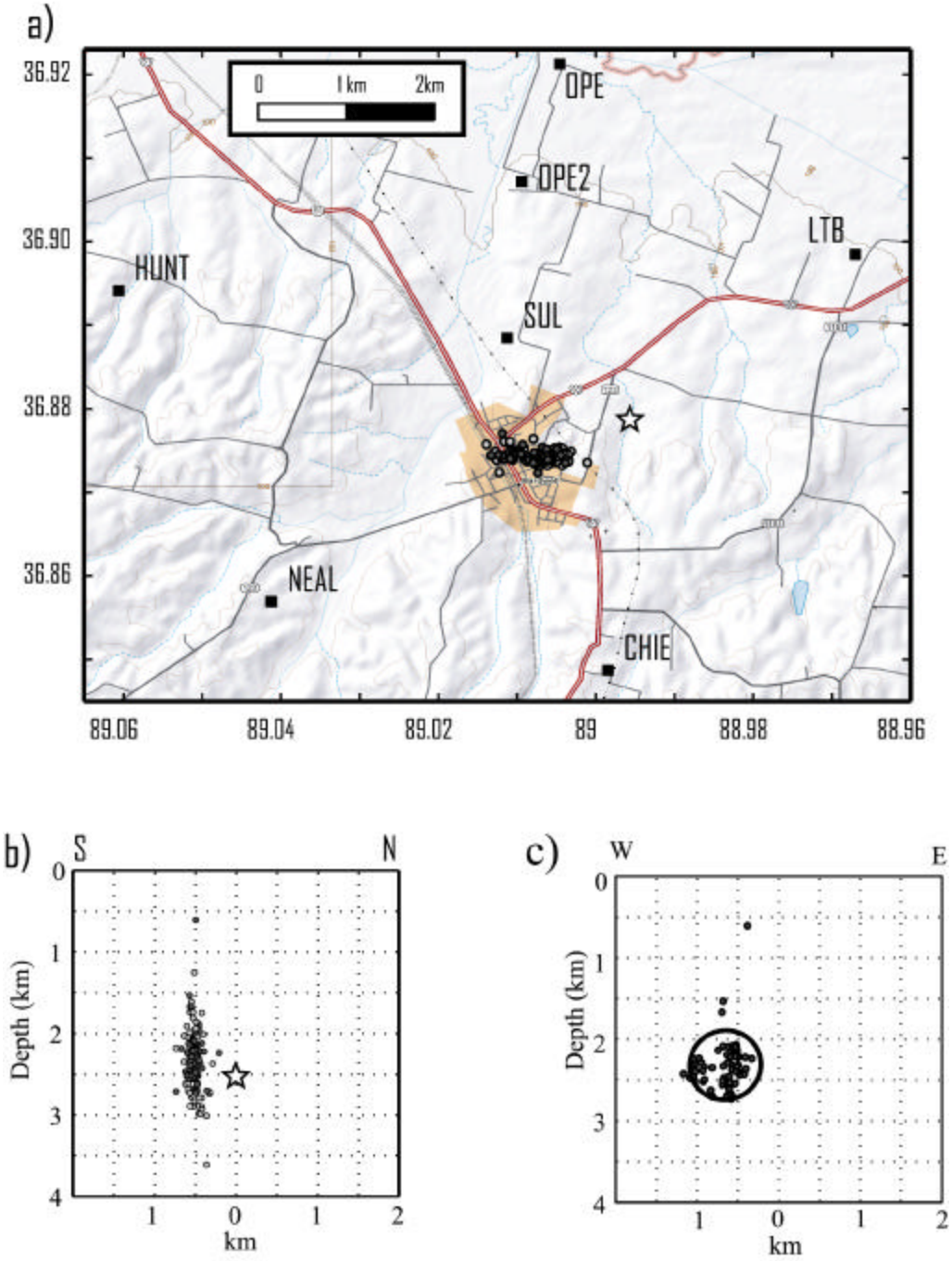

Figure 4. a). Broadband seismometers (*black squares*) deployed following the Bardwell earthquake. SUL is located at the initial estimate of the mainshock epicenter. The star gives the current estimate based on the regional network. Initial aftershock epicenters (*open circles*) and relocated epicenters (*dark circles*) clearly delineate an east trending zone approximately 1 km in length; b). North-south cross section shows aftershocks are consistent with a vertical east trending fault. The relocated hypocenters (*dark circles*) are more concentrated in the vertical dimension, and they are still consistent with a vertical fault, c). A circle of radius 0.44 km including 90% of the relocated aftershocks is displayed in this east-west cross section.

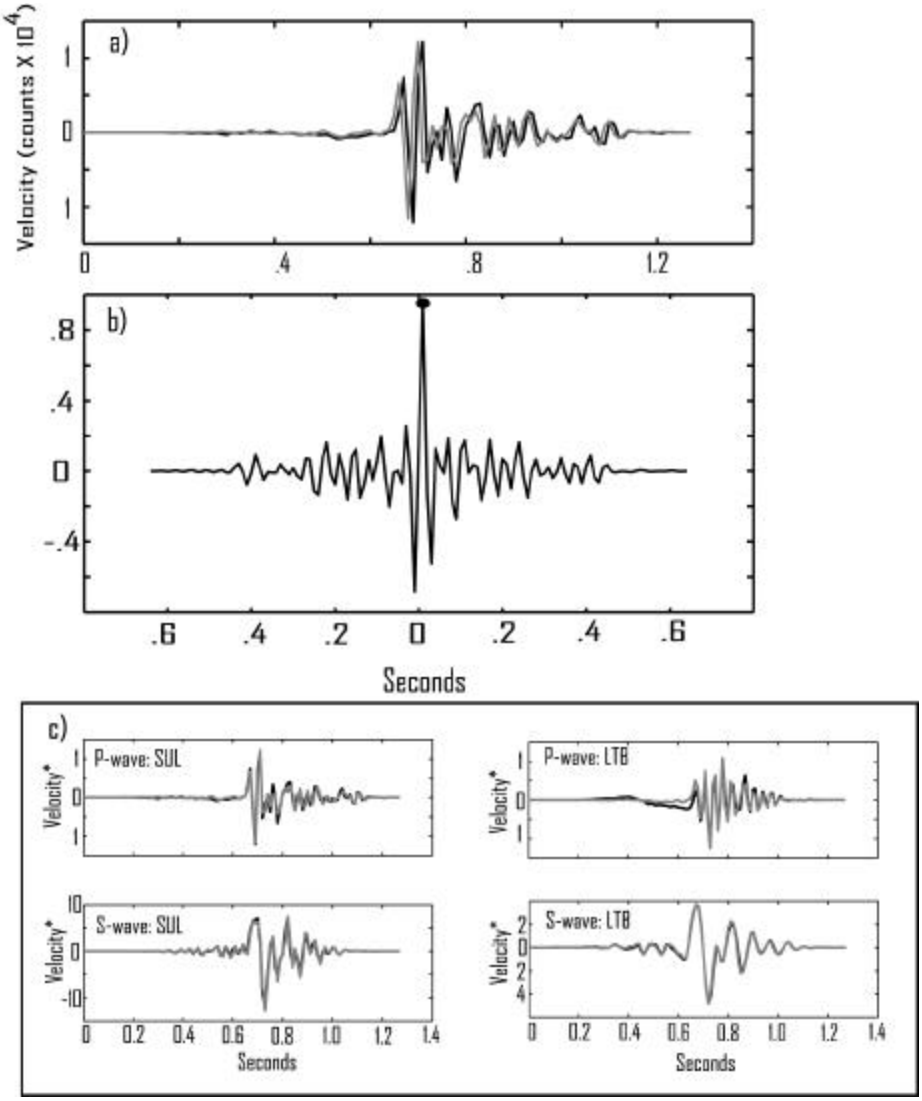

Figure 5. a) *P*-wave window for two events plotted relative to the adjusted arrival time (see text),. b) Normalized cross-correlation showing optimum lag time (differential travel time), c) Examples of *P*-waves and *S*-waves at two stations after adjustment by lag time.

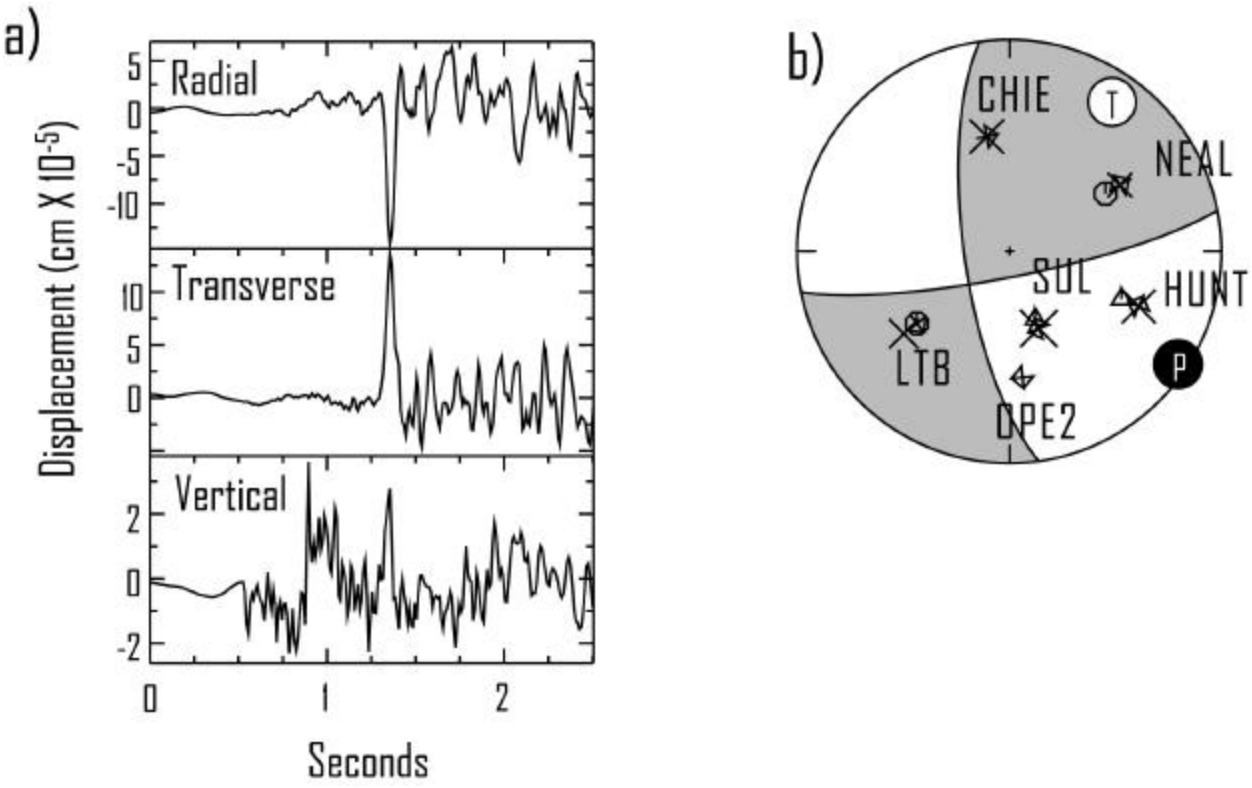

Figure 6. a) Displacement waveforms at station SUL for event #4. Horizontal waveforms are rotated to radial and transverse allowing identification of S wave polarity. B) Focal mechanism for event #4.

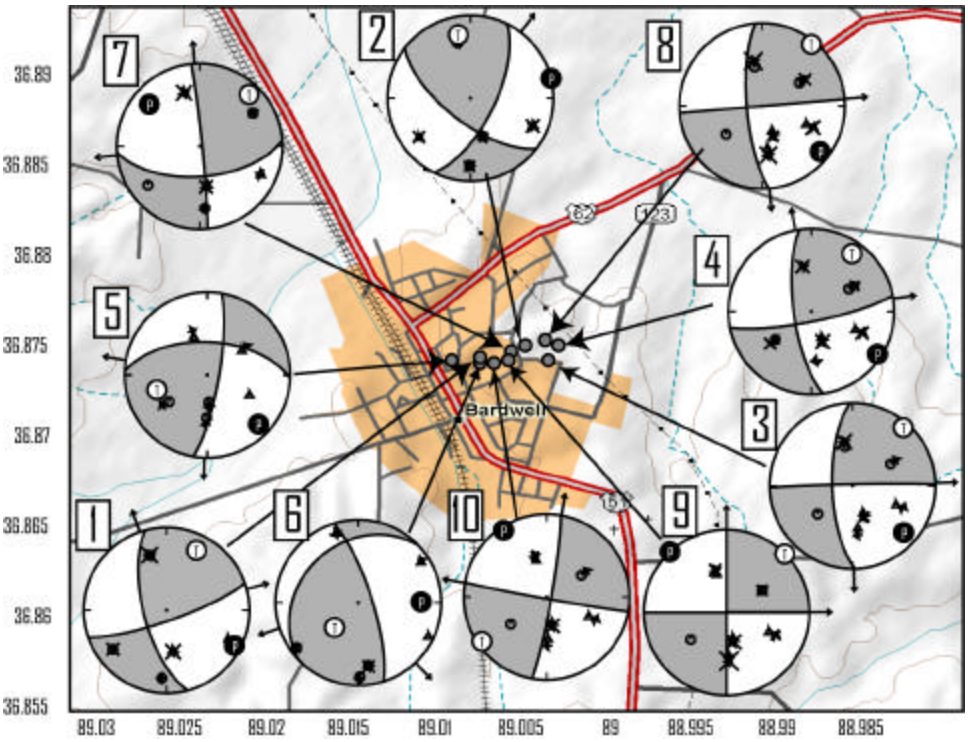

Figure 7. Aftershock focal mechanisms inferred from P- and S-wave polarities and ratios using the program **FOCMEC**. Event id is listed in Table 4.

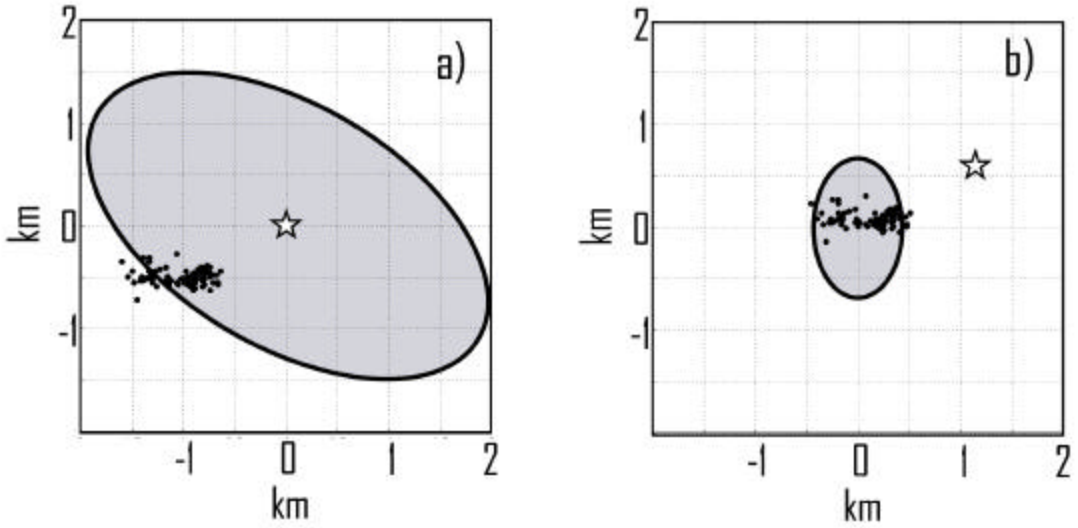

Figure 8. a) Projection onto a horizontal plane of the 95% confidence ellipsoid for the mainshock location. Note that many aftershocks occur outside of the specified confidence area. b). Projection onto a horizontal plane of the 95% confidence ellipsoid for an aftershock near the center of the distribution. Note that the mainshock location (*star*) is clearly outside the specified confidence area for this event.

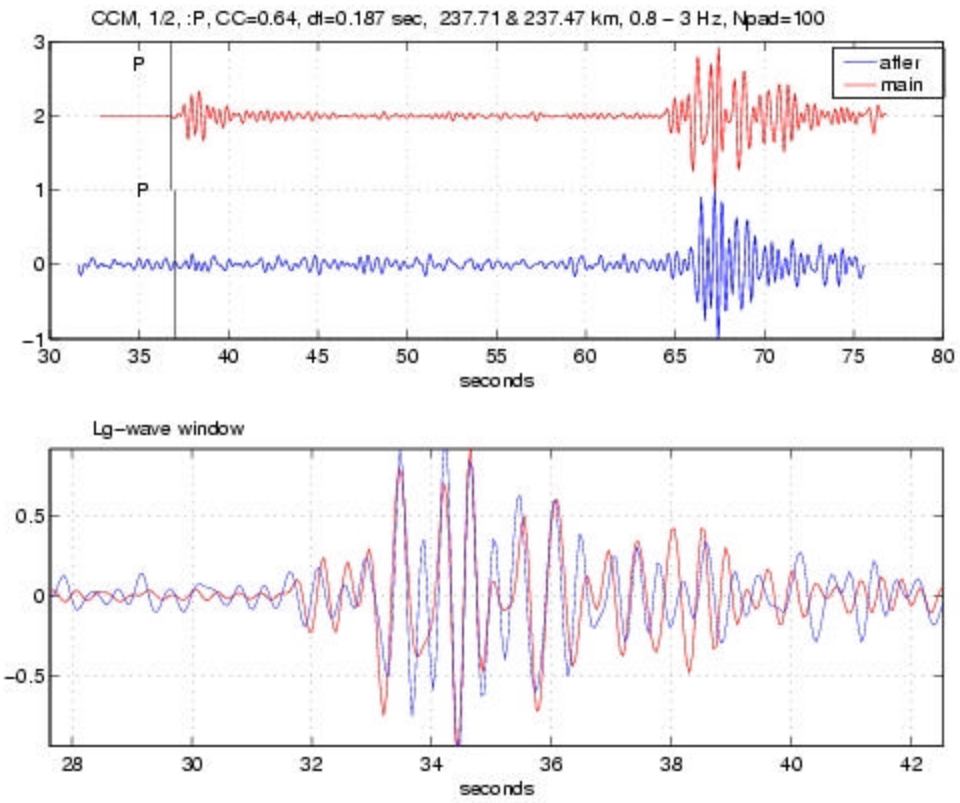

Figure 9. (*upper panel*) Regional EW-component records at CCM (Δ=238 km, AZ=304°) from the mainshock (*red trace*) and the largest aftershock on 06/08/2003 10:51 (M=2.4)(*blue trace*). Traces are plotted aligned to their *P*-wave travel times, (*lower panel*) Two traces are superposed after the waveform cross-correlation. Notice that cross-correlation is performed for 35 seconds time window, and the waveforms appears to be correlated to their largest amplitude arrivals (i.e., *Lg* arrivals) with correlation coefficient 0.64 and time lag of 0.187s, whereas the *P* waves are misaligned. Due to poor signal-to-noise ratio of *P* window for the aftershock, differential *S-P* times could not be determined, which could put constraint on the mainshock location relative to the master event.

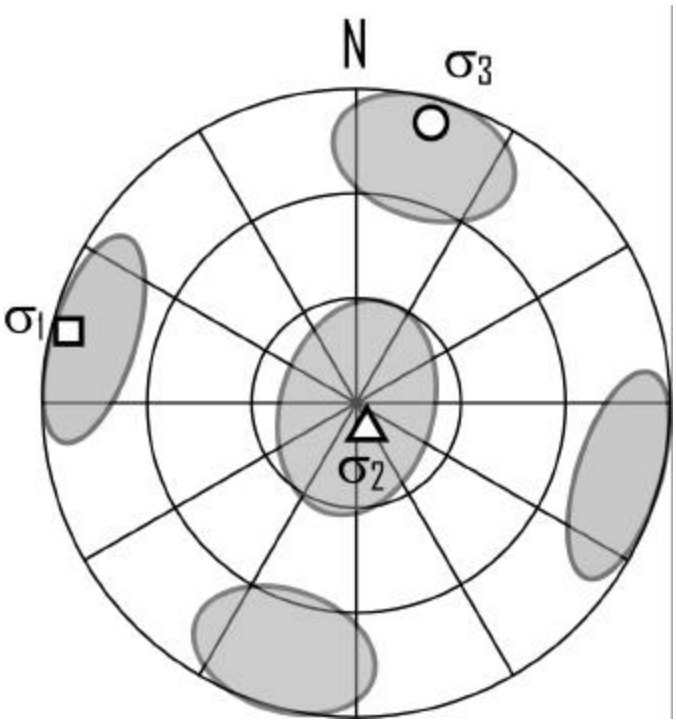

Figure 10. Maximum principal stress axis, σ_1 (*square*), intermediate axis, σ_2 (*triangle*), and least principal stress axis, σ_3 (*circle*) determined from inverting the focal mechanisms from 10 aftershocks. Notice that the orientation of the σ_1 is consistent with the *P* axis direction (118° or 298°) of the mainshock focal mechanism shown in Figure 2.

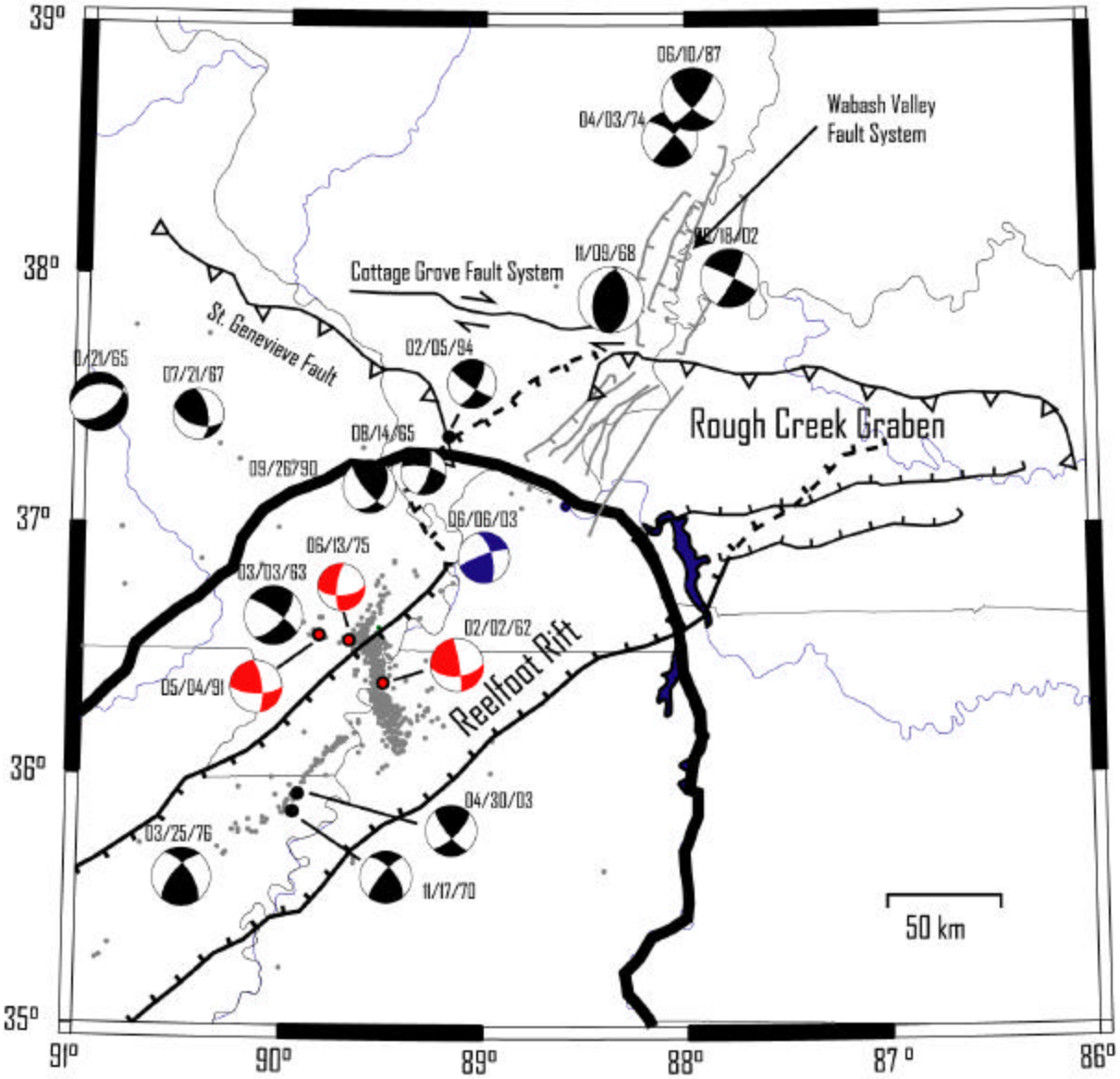

Figure 11. Focal mechanisms of the earthquakes that occurred in central U.S. since 1960s are plotted with color-coded beach balls (lower hemisphere projection of nodal planes). Solid lines show major geologic features around epicentral area with teeth on the downthrown side. These are from the south; the Reelfoot rift, a failed rift system in the northern Mississippi embayment, Rough Creek graben in western Kentucky, and the Wabash Valley fault system (WVFS) along southeastern Illinois-southwestern Indiana border. Tertiary limit that outlines the Mississippi embayment is indicated by *heavy solid line*. Earthquakes (*gray circles*) defining the New Madrid seismic zone (NMSZ) are shown to give the geometric orientation with the study area. The 6 June 2003 Bardwell, Kentucky earthquake is indicated by a *blue beach ball*. Focal mechanisms of earthquakes in the NMSZ with east-west trending nodal plane that have NE-ENE trending *P* axis are plotted by *red beach balls*. A comparison between Bardwell and New Madrid events, hence, indicates a strong perturbation in the stress field over a distance of about 60 km.